JOURNAL OF SPACECRAFT AND ROCKETS
Vol. 32, No. 6, November–December 1995

Ionosphere Ionization Effects on Sheath Structure Around a High-Voltage Spacecraft

Mengu Cho*
Kobe University, Nada-ku, Kobe 657, Japan

The electric sheath structure around a cylindrical spacecraft whose surface is biased to a high positive potential and surrounded by a water-vapor cloud in the ionosphere is studied. A small degree of ionization collision inside the sheath leads to an explosive sheath expansion, because the electric sheath tries to compensate for the loss of negative charge by attracting more electrons. An expression for the critical neutral density above which the sheath explosion occurs is derived. For typical conditions, the critical neutral density lies between 10^{16} and 10^{18} m^{-3}. Monte Carlo Particle-in-Cell simulation is done to check the validity of the expression. The simulation result shows the expression gives a reasonable prediction of the critical neutral density with the least computational time.

Nomenclature

$\boldsymbol{B}$ = magnetic field, G
$\boldsymbol{E}$ = electric field, V/m
L = characteristic length of system, m
m = particle mass, kg
n = number density, m^{-3}
n_{nc} = critical neutral density for explosive sheath expansion, m^{-3}
n_∞ = electron density of ambient Maxwellian plasma, m^{-3}
n_0 = electron density at sheath edge, m^{-3}
Q_+ = net positive charge inside sheath per unit length of cylinder, C/m
Q_- = net negative charge inside sheath per unit length of cylinder, C/m
r_p = cylinder radius, m
r_s = sheath radius, m
T = temperature, eV
v = velocity, m/s
v_d = spacecraft orbital velocity, m/s
v_0 = electron radial velocity at sheath edge, m/s
λ_D = Debye length of ambient Maxwellian plasma, m
ξ = nondimensional neutral density, $n_n \sigma_i r_p$
σ_i = ionization collision cross section, m^2
ϕ_p = spacecraft surface potential, V
χ_s = nondimensional sheath radius, r_s/r_p
ω_{pe} = electron plasma frequency of ambient Maxwellian plasma, rad/s

Subscripts

ai = ambient ion
e = electron
i = ion
n = neutral
p = plasma
r = radial direction
si = secondary ion
z = axial direction
θ = azimuthal direction

Presented as Paper 94-2449 at the AIAA 25th Plasmadynamics and Lasers Conference, Colorado Springs, CO, June 20–23, 1994; received July 20, 1994; revision received May 17, 1995; accepted for publication May 18, 1995.

*Research Associate, Division of System Science, The Graduate School of Science and Technology, 1-1 Rokko-dai; currently Teaching Associate, International Space University, Parc d'Innovation, Boul. Gonthier d'Andernach, 67400 Illkirch, France. E-mail: cho@isu.isunet.edu. Member AIAA.

Introduction

THE use of high power in future space missions calls for high-voltage power generation and transmission, typically higher than 100 V. Operation at high voltage, however, causes serious environmental interaction between the spacecraft and the ionospheric plasma. A key factor that determines the nature of the spacecraft–plasma interaction is the floating potential of the spacecraft. The positive-potential part of the spacecraft conducting surface collects electrons, and the negative part collects ions. At the steady state, the floating potential of the spacecraft ground is determined so that the ion and electron currents cancel each other. Therefore, once we know a formula to calculate the electron and ion currents for a given surface potential of the spacecraft, we know the floating potential of the spacecraft. Despite efforts by many people through more than three decades, we have not yet established a fundamental theory of current collection by a spacecraft.

The parameters that we encounter in the present issue are the plasma density (n_p), electron temperature (T_e), ion temperature (T_i), characteristic length of spacecraft (L), magnetic field ($\boldsymbol{B}$), neutral density (n_n), orbital velocity (v_d), and others. The parameter ranges of present interest are $n_p = 10^{10}$–10^{12} m^{-3}, $T_e = 0.1$–0.2 eV, $T_i = 0.02$–0.2 eV, $L = 0.1$–100 m, $|\boldsymbol{B}| = 0$–0.5 G, $n_n = 10^{14}$–10^{20} m^{-3}, and $v_d = 8$ km/s. An extensive review on the subject of current collection by an object in space plasma is given in Ref. 1. For the first four parameters (n_p, T_e, T_i, and L) a collisionless probe theory that integrates the Vlasov equation including the self-consistent space charge has been already established (see, for example, Ref. 2). If we include the geomagnetic field, the theoretical treatment becomes increasingly difficult, and only the case where the Debye length approaches infinity can be analyzed theoretically. Beyond this, numerical simulation is the only feasible method to predict the current collection for a given set of parameters.

Besides the complex dynamics of parameter interactions, there is a fundamental question yet to be answered, whether steady-state current collection is ever possible. It is no doubt that the current fluctuates with some amplitude and frequencies corresponding to the basic plasma oscillations. However, we are not sure the fluctuation is stable, especially when the spacecraft potential is high and the spacecraft is surrounded by neutral gas cloud.[1] It is not true that the vicinity of spacecraft is high vacuum, especially when it is emitting various neutral gases into space via thruster firing or outgassing. One report shows the neutral density around the spacecraft can become as high as 10^{18} m^{-3} when the thruster is fired for the attitude control.[3] This number becomes higher at points closest to the neutral contamination source. In such a situation, if there is a mechanism that enhances the plasma current, such as ionization or secondary electron emission from the spacecraft surface, a large transient discharge current can flow into the spacecraft, giving various undesired side effects on the spacecraft operation, such as

electromagnetic interference or surface deterioration. The purpose of the present paper is to study whether stable current collection is possible when ionization collision within the sheath is not negligible.

Ionization collisions inside the sheath create additional pairs of attracted and repelled particles. If the increase of the attracted species is smaller than that of the repelled species, the sheath must collect more attracted species to compensate for the difference. This difference occurs when one species stays inside the sheath longer than the other as a result of various mechanisms, such as the mass difference between electrons and ions or trapping of electrons due to the geomagnetic field. Then the sheath boundary expands outward to collect more attracted species. If the increase of attracted species is larger, the sheath boundary shrinks inward. The current flowing into the spacecraft is the sum of the current from the sheath boundaries and the current due to secondary particles created inside the sheath via ionization.

Current collection by a positively biased spacecraft has been studied by several authors in conjunction with high-voltage space experiments.[4–6] Cooke and Katz[7] studied explosive sheath expansion into unmagnetized ionospheric plasma. They analytically determined the critical neutral density for the explosive expansion as

$$n_n = \sigma^{-1}\lambda_D^{-1}(\kappa T/e\phi_p)^{\frac{3}{4}}\sqrt{m_e/m_i}\,\alpha \tag{1}$$

where α is an anode factor that accounts for the difference of the spacecraft (probe) geometry. The anode factor is unity for planar geometry. In Ref. 7 numerical simulation was also carried out with a fluid simulation code for planar and spherically symmetric systems. But the determination of the anode factor for the spherical case was left for more accurate evaluation. Ma and Schunk[8] solved three-dimensional fluid equations and the Poisson equation to study the ionization surrounding a sphere held at a positive potential of 10,000 V. The result of Ref. 8 shows that a toroidal discharge occurs around the biased sphere due to efficient ionization by $\boldsymbol{E} \times \boldsymbol{B}$-drifting electrons. For higher voltages, the toroidal discharge tends to be more spherical. These results agree qualitatively with the laboratory experiments of Refs. 9 and 10. In those experiments diffusive volume breakdown between the chamber wall and the highly positively biased sphere was observed at $B > 2$ G and $p > 10^{-4}$ torr. Antoniades et al.[11] attributed the breakdown to trapping of secondary electrons from the chamber wall by the $\boldsymbol{E} \times \boldsymbol{B}$ drift. So far no space experiment has shown this phenomena.[4,6]

Cho[12] studied a negative-bias case where an infinite-length cylinder whose axis is parallel to the geomagnetic field is surrounded by argon gas. In Ref. 12, secondary electrons due to ion bombardment on the conducting spacecraft surface are assumed. Then the secondary electrons efficiently ionize the neutral atoms while they undergo $\boldsymbol{E} \times \boldsymbol{B}$ drift inside the sheath. However, Ref. 12 neglected the unsteady motion of sheath, in particular the effect of space charge due to the secondary ions inside the sheath.

In the present paper, we study current collection by a cylindrical spacecraft biased to a positive potential in the unmagnetized ionospheric plasma. When the spacecraft surface is biased to a positive potential, it is surrounded by an electric sheath. We consider a case where the Debye length λ_D is much less than the cylinder radius r_p, that is, the sheath is space-charge-limited. The electrons that cross the sheath boundary from the ambient are collected by the spacecraft, and the sheath boundary is determined so that the negative charge inside the sheath cancels the positive potential of the spacecraft.

When the spacecraft is surrounded by a neutral cloud and ionization occurs inside the sheath, the secondary ions accumulate inside the sheath because they move slower and stay longer in the sheath than the secondary electrons. The sheath boundary expands outward to compensate for the loss of the negative charge. As the neutral density increases, we have more secondary ions, and the sheath must collect more electrons from the ambient by extending the boundary further. Above a certain neutral density, we might have infinite sheath boundary expansion, and we call that value the critical neutral density in the present paper.

The same subject was previously studied in Ref. 7, and Eq. (1) was given as the expression for the critical neutral density for planar geometry. But Ref. 7 does not address cylindrically symmetric systems. In the present paper, we derive an expression similar to Eq. (1) for cylindrical geometry, including the evaluation of the anode factor α. We also examine the validity of the expression with Monte Carlo Particle-in-Cell (MC-PIC) code, which employs fewer approximations than the fluid code used in Ref. 7. For the present case, the ionization probability within the sheath is much less than 1, though sheath explosion is still possible. Then the current collected by the spacecraft is linearly proportional to the surface area of the sheath boundary, i.e., the radius of the sheath boundary. Therefore, the study of the sheath radius is equivalent to the study of current collection as long as they remain stable.

Initially, we will conduct an analytical study and calculate the sheath radius for a given set of neutral density and other parameters. We also will derive an expression for the critical neutral density. Then we will use the one-dimensional MC-PIC code to check the validity of the expression.

One-Dimensional Cold-Fluid Analysis

We first make a simplified cold-fluid analysis of the system shown in Fig. 1. The system has a cylinder of radius r_p at the center, and spatial variation occurs only in the r direction. Between the spacecraft (or probe) surface at r_p and the sheath boundary at r_s, the neutral density n_n is assumed to be uniform. The purpose of the present analysis is to find an analytical expression that relates the sheath boundary radius r_s and the uniform neutral density n_n.

Before proceeding to further analysis, we first clarify the meanings of sheath, sheath boundary, and presheath as used in this paper. When a sheath is formed around a positively biased spacecraft, electrons are attracted to the spacecraft and ions are repelled. Outside the edge of the presheath, the plasma density is n_∞, the temperatures are T_e and T_i, and the plasma has no directed velocity, that is, $v_e = v_i = 0$. Charge neutrality holds in the presheath, though the plasma density decreases gradually. We define the sheath boundary as the point beyond which charge neutrality no longer holds and the electron density is higher than the ion density. In the present paper, we consider only the region between the cylinder surface and the sheath boundary. The potential increases gradually from zero at the edge of the presheath to a potential of the order of the plasma temperature (0.1–0.2 eV) at the sheath boundary. Electrons are gradually accelerated inside the presheath and have the Bohm velocity $\sqrt{(\kappa T_e/m_e)}$ at the sheath boundary. The plasma density falls gradually in the presheath from the value n_∞ outside the presheath. According to Ref. 13, the plasma density decreases to $0.4n_\infty$ at the sheath boundary.

At the sheath boundary, we consider the following boundary conditions:

$$\phi(r_s) = 0 \tag{2}$$

$$\left.\frac{\partial \phi}{\partial r}\right|_{r_s} = 0 \tag{3}$$

$$n_e(r_s) = n_0 = 0.4n_\infty \tag{4}$$

$$n_{ai}(r_s) = n_0 \tag{5}$$

$$v_e(r_s) = v_0 = -\sqrt{\frac{\kappa T_e}{m_e}} \tag{6}$$

At the cylinder surface, the boundary conditions are

$$\phi(r_s) = \phi_p \tag{7}$$

$$n_{si}(r_p) = 0 \tag{8}$$

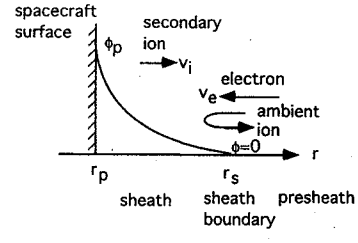

Fig. 1 Schematic picture of the system studied.

At the sheath boundary, the electric potential is of the order of the plasma temperature. Since we deal with the case where $\kappa T_e \ll e\phi_p$ in the present paper, we neglect the potential at the sheath boundary and approximate it by zero. The electric field at the sheath boundary is also finite. But since it is also much smaller than the field at the spacecraft surface, we neglect the field at r_s.

When an electric sheath is formed around a biased spacecraft, the net positive space charge per unit length of cylinder, Q_+, and the negative space charge per unit length of cylinder, Q_-, satisfy the following relation:

$$r_s \left.\frac{\partial\phi}{\partial r}\right|_{r_s} - r_p \left.\frac{\partial\phi}{\partial r}\right|_{r_p} = \frac{-1}{\epsilon_0}(Q_+ + Q_-) \tag{9}$$

where the net charges are given by

$$Q_- = -e\int_{r_p}^{r_s} n_e r\,\mathrm{d}r \tag{10}$$

$$Q_+ = e\int_{r_p}^{r_s} (n_{si} + n_{ai}) r\,\mathrm{d}r \tag{11}$$

Equation (9) is derived directly by integrating the Poisson equation in a cylindrical coordinate from r_p to r_s. In Eq. (11) the ions are divided into two groups. One is the group of ions born in the sheath due to ionization collisions, whose density is denoted by n_{si}, and the other is the group of ions coming from outside the presheath, n_{ai}.

From the boundary condition given by Eq. (3), the first term on the left-hand side (LHS) of Eq. (9) vanishes. To pursue the analytical approach to obtain the relation between r_s and n_n, we need a functional formula to describe the electric field at the cylinder surface r_p. We approximate the electric field at r_p by

$$\left.\frac{\partial\phi}{\partial r}\right|_{r_p} = -\frac{\phi_p}{r_p\,\ell_n(r_s/r_p)} \tag{12}$$

This field is equivalent to the surface field if the voltage ϕ_p is biased between the coaxial cylindrical electrode with no space charge inside. Strictly speaking, this approximation is not correct and underestimates the field strength at the cylinder surface, because we are dealing with a space-charge-dominated problem. In the Appendix, we numerically calculate the surface field for various cases and discuss the validity of Eq. (12). Using Eq. (12), we can rewrite Eq. (9) as follows:

$$-\frac{\epsilon_0\phi_p}{\ell_n(r_s/r_p)\,r_p} = Q_+ + Q_- \tag{13}$$

For a given set of ϕ_p and r_p, the net charges Q_-, Q_+ and the field strength at r_s are functions of n_n and r_s. Then we can write the total differential of Eq. (13) as follows:

$$\frac{\epsilon_0\phi_p}{[\ell_n(r_s/r_p)]^2 r_s}\,\mathrm{d}r_s = \frac{\partial Q_+}{\partial r_s}\,\mathrm{d}r_s + \frac{\partial Q_+}{\partial n_n}\,\mathrm{d}n_n + \frac{\partial Q_-}{\partial r_s}\,\mathrm{d}r_s + \frac{\partial Q_-}{\partial n_n}\,\mathrm{d}n_n \tag{14}$$

Rewriting this equation, we obtain

$$\frac{\mathrm{d}r_s}{\mathrm{d}n_n} = \frac{\dfrac{\partial Q_+}{\partial n_n} + \dfrac{\partial Q_-}{\partial n_n}}{\dfrac{\epsilon_0\phi_p}{[\ell_n(r_s/r_p)]^2 r_s} - \dfrac{\partial Q_+}{\partial r_s} - \dfrac{\partial Q_-}{\partial r_s}} \tag{15}$$

This gives the degree of sheath expansion for a unit increase of the neutral density. The purpose of this section is to derive an explicit formula for $\mathrm{d}r_s/\mathrm{d}n_n$ to integrate numerically for a given set of parameters and find the condition where the gradient $\mathrm{d}r_s/\mathrm{d}n_n$ becomes infinite, that is, explosive sheath expansion occurs.

Now we derive expressions for Q_+ and Q_-. The current continuity equations in the cylindrical system are given by

$$\frac{1}{r}\frac{\partial}{\partial r}(r n_e v_e) = -n_n\sigma_i v_e n_e \tag{16}$$

$$\frac{1}{r}\frac{\partial}{\partial r}(r n_{si} v_{si}) = -n_n\sigma_i v_e n_e \tag{17}$$

where $-n_n\sigma_i v_e$ on the right-hand side (RHS) corresponds to the ionization frequency, and the negative sign comes from the fact that the electron radial velocity is negative (see Fig. 1). In the present paper, we are concerned whether the steady-state solution exists or not. The transient behavior of the sheath structure is beyond the scope of the present paper, and we neglect the unsteady term in the continuity equations.

Integrating Eq. (16) from r_s to r and Eq. (17) from r_p to r, we obtain

$$n_e v_e r = (n_0 v_0 r_s)\exp[-n_n\sigma_i(r - r_s)] \approx [1 - n_n\sigma_i(r - r_s)](n_0 v_0 r_s) \tag{18}$$

$$n_{si} v_{si} r = (n_0 v_0 r_s)\{\exp[-n_n\sigma_i(r - r_p)] - 1\}\exp[-n_n\sigma_i(r_p - r_s)] \approx (n_0 v_0 r_s) n_n\sigma_i(r_p - r) \tag{19}$$

where $n_n\sigma_i r \ll 1$ is assumed. For the ambient ion density n_{ai}, we assume the Boltzmann distribution, which is given by

$$n_{ai}(r) = n_0\exp\left(-\frac{e\phi(r)}{\kappa T_{ai}}\right) \tag{20}$$

Then, we substitute Eqs. (18–20) into Eqs. (10) and (11) and obtain

$$Q_- = -e n_0 v_0 r_s\left(\int_{r_p}^{r_s}\frac{1}{v_e}\,\mathrm{d}r + n_n\sigma_i\int_{r_p}^{r_s}\frac{r_s - r}{v_e}\,\mathrm{d}r\right) \tag{21}$$

$$Q_+ = e n_0 v_0 r_s n_n\sigma_i\int_{r_p}^{r_s}\frac{r_p - r}{v_{si}}\,\mathrm{d}r + e n_0\int_{r_p}^{r_s} r\exp\left(-\frac{e\phi}{\kappa T_{ai}}\right)\mathrm{d}r \tag{22}$$

The first term in Q_- is the contribution due to the ambient electrons, and the second term accounts for the increase due to ionization. The first term in Q_+ is the contribution due to the secondary ions, and the second term is due to the ambient ions.

Taking the partial derivatives of Q_- and Q_+ with respect to r_s and n_n, we obtain

$$\frac{\partial Q_-}{\partial r_s} = -e n_0 v_0\left(\int_{r_p}^{r_s}\frac{1}{v_e}\,\mathrm{d}r + n_n\sigma_i r_s\int_{r_p}^{r_s}\frac{2 - r/r_s}{v_e}\,\mathrm{d}r + \frac{r_s}{v_0}\right) \approx -e n_0 v_0\int_{r_p}^{r_s}\frac{1}{v_e}\,\mathrm{d}r - e n_0 r_s \tag{23}$$

$$\frac{\partial Q_+}{\partial r_s} = e n_0 v_0 n_n\sigma_i\left(\int_{r_p}^{r_s}\frac{r_p - r}{v_{si}}\,\mathrm{d}r + \frac{r_s(r_p - r_s)}{v_{si}(r_s)}\right) + e n_0 r_s \tag{24}$$

$$\frac{\partial Q_-}{\partial n_n} = -e n_0 v_0 r_s\sigma_i\int_{r_p}^{r_s}\frac{r_s - r}{v_e}\,\mathrm{d}r \tag{25}$$

$$\frac{\partial Q_+}{\partial n_n} = e n_0 v_0 r_s\sigma_i\int_{r_p}^{r_s}\frac{r_p - r}{v_{si}}\,\mathrm{d}r \tag{26}$$

In Eq. (23), $n_n\sigma_i r_s \ll 1$ is used to neglect the contribution due to the secondary electrons to $\partial Q_-/\partial r_s$. Substituting the above partial derivatives into Eq. (15), we obtain

$$\frac{dr_s}{dn_n} = \frac{en_0 v_0 r_s \sigma_i \left(\int_{r_p}^{r_s} \frac{r_p - r}{v_{si}} dr - \int_{r_p}^{r_s} \frac{r_s - r}{v_e} dr \right)}{\frac{\epsilon_0 \phi_p}{[\ell_n(r_s/r_p)]^2 r_s} + en_0 v_0 \left[\int_{r_p}^{r_s} \frac{1}{v_e} dr - n_n \sigma_i \left(\int_{r_p}^{r_s} \frac{r_p - r}{v_{si}} dr + \frac{r_s(r_p - r_s)}{v_{si}(r_s)} \right) \right]} \tag{27}$$

where the last terms of the RHSs of Eqs. (23) and (24) cancel each other.

We cannot yet integrate Eq. (27), because the electron and ion velocities are not given in functional forms yet. We now derive an approximate formula for v_{si} to substitute into Eq. (27). At a point r, there are multiple groups of ions, which are created at different points between r_p and r. An ion born at r' is accelerated to a velocity of $v_{si}(r, r')$ at r, which is given by

$$\frac{1}{2} v_{si}^2(r, r') = \int_{r'}^{r} -\frac{e}{m_i} \frac{\partial}{\partial r} \phi \, dr'' \tag{28}$$

This equation merely states the energy conservation where ion–neutral collisions are neglected and the ion is assumed to be born with zero energy. We approximate the acceleration by

$$-\frac{e}{m_i} \frac{\partial}{\partial r} \phi = \frac{e\phi_p}{m_i \ell_n(r_s/r_p) r} \tag{29}$$

which leads to the potential approximated by the solution of the Laplace equation between r_p and r_s. We substitute Eq. (29) into Eq. (28) and integrate to obtain

$$v_{si}(r, r') = \sqrt{\frac{2e\phi_p}{m_i \ell_n(r_s/r_p)}} \left[\ell_n \left(\frac{r}{r'} \right) \right]^{\frac{1}{2}} \tag{30}$$

In the range between r' and $r' + dr'$, ions are created at a rate of $(-n_0 v_0 r_s) n_n \sigma_i \, dr'$ per unit length of the cylinder. The contribution to the number of ions at r from the group born between r' and $r' + dr'$ is

$$\delta n_i(r, r') \, dr' = \frac{(-n_0 v_0 r_s) n_n \sigma_i \, dr'}{v(r, r')}. \tag{31}$$

Then the average velocity of ion at r is given by summing the contribution from all the groups born before r and is written as

$$\begin{aligned} \langle v_{si}(r) \rangle &= \frac{\int_{r_p}^{r} v_{si}(r, r') \, \delta n_i(r, r') \, dr'}{\int_{r_p}^{r} \delta n_i(r, r') \, dr'} \\ &= \frac{\int_{r_p}^{r} [v_{si}(r, r')(-n_0 v_0 r_s) n_n \sigma_i / v_{si}(r, r')] \, dr'}{\int_{r_p}^{r} \left[(-n_0 v_0 r_s) n_n \sigma_i / v_{si}(r, r') \right] dr'} \\ &= \frac{r - r_p}{\int_{r_p}^{r} (1/v_{si}(r, r')) \, dr'} \end{aligned} \tag{32}$$

where $\delta n_i(r, r')$ is the weighting for the group of particles born between r' and $r' + dr'$ in calculating the average at r. We substitute Eq. (30) into into Eq. (32) and after some algebra obtain

$$\langle v_{si}(r) \rangle = \frac{1}{2} \sqrt{\frac{2e\phi_p}{m_i \ell_n(r_s/r_p)}} \frac{r - r_p}{r \, \mathrm{Erf}[\sqrt{\ell_n(r/r_p)}]} \tag{33}$$

where the error function $\mathrm{Erf}(x)$ is defined as

$$\mathrm{Erf}(x) \equiv \int_0^x \exp(-t^2) \, dt \tag{34}$$

and

$$\int_{r_p}^{r_s} \left[\ell_n \left(\frac{r}{r'} \right) \right]^{-\frac{1}{2}} dr' = 2r \int_0^{\sqrt{\ell_n(r/r_p)}} \exp(-t^2) \, dt \tag{35}$$

is used.

The electron velocity $v_e(r)$ is given by a similar formula to Eq. (28):

$$v_e^2(r) - v_0^2 = \int_{r_s}^{r} \frac{e}{m_e} \frac{\partial}{\partial r} \phi \, dr' \tag{36}$$

Again, we have neglected the effect of collisions on the electron momentum increase. The effect of the secondary electrons that have smaller energy than the primary electrons is also neglected, because the fraction of the secondary electrons is of the order of $n_n \sigma (r_s - r) \ll 1$ as shown in Eq. (18). Substituting Eq. (29) into Eq. (36), we obtain the following formula for the electron velocity:

$$\begin{aligned} v_e(r) &= -\sqrt{\frac{2e\phi_p}{m_e \ell_n(r_s/r_p)}} \left[\frac{m_e \ell_n(r_s/r_p)}{2e\phi_p} v_0^2 + \ell_n \left(\frac{r_s}{r} \right) \right]^{\frac{1}{2}} \\ &\approx -\sqrt{\frac{2e\phi_p}{m_e \ell_n(r_s/r_p)}} \sqrt{\ell_n \left(\frac{r_s}{r} \right)} \end{aligned} \tag{37}$$

The first term in the bracket on the RHS has been neglected because $\kappa T_e / e\phi_p \ll 1$.

Using the average ion velocity $\langle v_{si}(r) \rangle$ for $v_{si}(r)$ in Eq. (27), the differential equation is rewritten as

$$\begin{aligned} \frac{dr_s}{dn_n} = \frac{en_0 v_0 r_s \sigma_i}{\sqrt{\frac{2e\phi_p}{m_i \ell_n(r_s/r_p)}}} & \left\{ -\int_{r_p}^{r_s} 2r \, \mathrm{Erf} \left[\sqrt{\ell_n \left(\frac{r}{r_p} \right)} \right] dr \right. \\ & \left. + \sqrt{\frac{m_e}{m_i}} \int_{r_p}^{r_s} \frac{r_s - r}{\sqrt{\ell_n(r_s/r)}} dr \right\} \Bigg/ \left[\frac{\epsilon_0 \phi_p}{[\ell_n(r_s/r_p)]^2 r_s} \right. \\ & - \frac{en_0 v_0}{\sqrt{\frac{2e\phi_p}{m_i \ell_n(r_s/r_p)}}} \left(\sqrt{\frac{m_e}{m_i}} \int_{r_p}^{r_s} \frac{1}{\sqrt{\ell_n(r_s/r)}} dr \right. \\ & - n_n \sigma_i \left\{ \int_{r_p}^{r_s} 2r \, \mathrm{Erf} \left[\sqrt{\ell_n \left(\frac{r_s}{r} \right)} \right] dr \right. \\ & \left. \left. \left. + 2r_s^2 \, \mathrm{Erf} \left[\sqrt{\ell_n \left(\frac{r_s}{r} \right)} \right] \right\} \right) \Bigg] \end{aligned} \tag{38}$$

We normalize the sheath radius r_s and the neutral density n_n as

$$\chi_s = \frac{r_s}{r_p} \tag{39}$$

$$\xi = n_n \sigma_i r_p \tag{40}$$

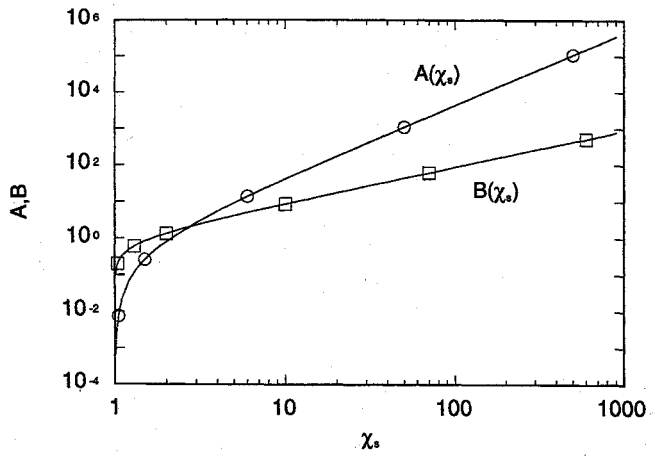

Fig. 2 Nondimensional functions $A(\chi_s)$ (circles) and $B(\chi_s)$ (squares).

Then Eq. (38) is rewritten in a nondimensional form as follows:

$$\frac{d\chi_s}{d\xi} = \frac{A(\chi_s) - D_2 C(\chi_s)}{D_1 D_2 / \left[(\ell_n \chi_s)^{\frac{5}{2}} \chi_s^2\right] + D_2(B(\chi_s)/\chi_s) - [A(\chi_s)/\chi_s + B(\chi_s)]\xi} \tag{41}$$

where D_1 and D_2 are constants given by

$$D_1 = \frac{1}{\sqrt{2}} \frac{\epsilon_0 \kappa T_e}{n_0 e^2 r_p^2} \left(\frac{e\phi_p}{\kappa T_e}\right)^{\frac{3}{2}} = \frac{1}{0.4\sqrt{2}} \left(\frac{\lambda_D}{r_p}\right)^2 \left(\frac{e\phi_p}{\kappa T_e}\right)^{\frac{3}{2}} \tag{42}$$

$$D_2 = \sqrt{\frac{m_e}{m_i}} \tag{43}$$

where λ_D is the Debye length at the ambient plasma, for which the plasma density is n_∞, and the electron temperature is κT_e, that is,

$$\lambda_D^2 = \frac{\epsilon_0 \kappa T_e}{n_\infty e^2} \tag{44}$$

The factor of 0.4 in Eq. (42) comes from the fact $n_0 = 0.4 n_\infty$. Also, $A(\chi_s)$, $B(\chi_s)$, and $C(\chi_s)$ in Eq. (41) are nondimensional functions of χ_s given by

$$A(\chi_s) = \int_1^{\chi_s} \chi \,\mathrm{Erf}(\sqrt{\ell_n \chi})\, d\chi \tag{45}$$

$$B(\chi_s) = \chi_s \,\mathrm{Erf}(\sqrt{\ell_n \chi_s}) \tag{46}$$

$$C(\chi_s) = \chi_s^2 [\mathrm{Erf}(\sqrt{\ell_n \chi_s}) - \frac{1}{\sqrt{2}} \mathrm{Erf}(\sqrt{2\ell_n \chi_s})] \tag{47}$$

Integrating by parts, the function $A(\chi_s)$ is rewritten as

$$A(\chi_s) = \frac{1}{2}\left(\chi_s B(\chi_s) - \int_0^{\sqrt{\ell_n(\chi_s)}} \exp(t^2)\, dt\right) \tag{48}$$

We plot the functions $A(\chi_s)$ and $B(\chi_s)$ in Fig. 2. In the limit of thick sheath, $\chi_s \gg 1$, the functions approach

$$A(\chi_s) = \frac{\sqrt{\pi}}{4} \chi_s^2 \tag{49}$$

$$B(\chi_s) = \frac{\sqrt{\pi}}{2} \chi_s \tag{50}$$

In the opposite limit of a thin sheath, $\chi_s - 1 \ll 1$, they approach

$$A(\chi_s) = \tfrac{1}{2}\left(\chi_s^2 \sqrt{\ell_n \chi_s} - \sqrt{\ell_n \chi_s}\right) = \tfrac{1}{2}(\chi_s + 1)(\chi_s - 1)^{\frac{3}{2}} \tag{51}$$

$$B(\chi_s) = \chi_s \sqrt{\ell_n \chi_s} = \chi_s \sqrt{\chi_s - 1} \tag{52}$$

where $\ell_n \chi_s \approx \chi_s - 1$ is used.

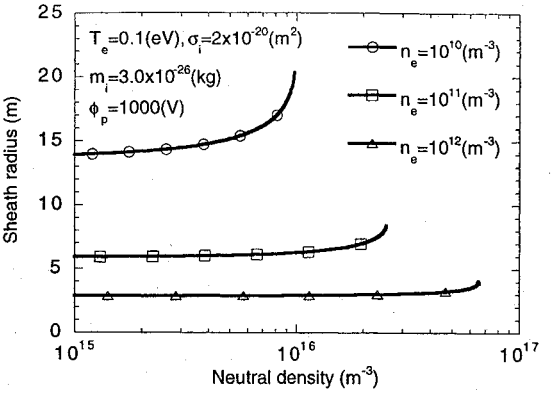

Fig. 3 Sheath radius vs neutral density for $r_p = 1$ m.

To integrate the differential equation (41) we need an initial value for χ_s at $\xi \to 0$. Since we are dealing with very high potential compared to T_e, the orbital motion can be neglected. In Appendix A, we calculate the sheath thickness by solving a simple set of cold-fluid equations. From the results, the sheath thickness is approximated by

$$\chi_s - 1 = 0.62 \times \left(\frac{-e n_0 v_0}{\epsilon_0 \sqrt{e/m_e}\, \phi_p^{\frac{3}{2}} / r_p^2}\right)^{-0.42} = 0.91 \left(\frac{\lambda_D}{r_p}\right)^{0.84} \left(\frac{e\phi_p}{\kappa T_e}\right)^{0.63} \tag{53}$$

where 0.91 comes from $0.62(n_0)^{-0.42} = 0.91(n_\infty)^{-0.42}$ and Eqs. (4), (6), and (44) have been used.

Finally we can numerically integrate the differential equation from $\xi = 0$ for a given set of n_∞, T_e, r_p, and ϕ_p. In Fig. 3, we plot the integrated curves of $r_s(n_n)$ for three different plasma densities, $n_\infty = 10^{10}$, 10^{11}, and 10^{12} m^{-3}, which correspond to low, medium, and high plasma density in the ionosphere, respectively. The other parameters in the figure are $r_p = 1$ m, $T_e = 0.1$ eV, $\sigma_i = 2\times10^{-20}$ m^2, $m_i = 3.0\times10^{-26}$ kg (water vapor), and $\phi_p = 1000$ V. The integration is done by the fourth-order Runge–Kutta method. At low neutral densities $n_n \le 10^{15}$ m^{-3}, the sheath radius varies only a little from the collisionless limits. As the neutral density increases, the sheath begins to expand. At the plasma density $n_\infty = 10^{10}$ m^{-3}, which gives the thickest sheath and the highest probability of ionization, the sheath increases rapidly as the neutral density approaches 1×10^{16} m^{-3}. At the neutral density of $n_n = 1.0 \times 10^{16}$ m^{-3}, the sheath radius becomes 20 m from the original 14 m, and the denominator in Eq. (41) becomes zero, that is, explosive sheath expansion occurs. The situation is similar for the other values of plasma density, though they are not as distinct as at $n_\infty = 10^{10}$ m^{-3}. The denominator becomes zero at the neutral density of $n_n = 3 \times 10^{16}$ m^{-3} and $n_n = 8 \times 10^{16}$ m^{-3} for the medium and high plasma densities.

The current collected by a unit length of the cylinder is given by substituting $r = r_p$ into Eq. (18) and multiplying it by e. Therefore, as the sheath expands infinitely, a large transient current flows into the spacecraft surface. In reality, however, the spacecraft cannot collect an infinite amount of current from the ionosphere. There is always a mechanism that saturates the current increase. For the present case under the unmagnetized assumption, the mechanism is either orbital limitation on the electron motion inside the sheath, or the resistivity of the spacecraft body, by which the large electron current drives the positive surface potential down. The orbital limitation begins to appear when the sheath radius increases to $r_s \approx r_p \sqrt{(e\phi_p/\kappa T_e)}$. For the case shown in Fig. 3, this number becomes $r_s \approx 100$ m. For $n_e = 10^{12}$ m^{-3}, the sheath radius of 100 m is more than 30 times the value at $n_n \to 0$. It is an interesting question whether the current is really orbit-limited at this value, because collision with neutrals, which is very probable within this distance, would mitigate the orbital limitation. Therefore, the current might grow until the effect of the spacecraft resistivity begins to appear.

It is worthwhile to seek an expression for the critical neutral density, that is, the density where the explosive sheath expansion occurs. It occurs when the denominator of Eq. (41) becomes zero. Equating the denominator to zero, we have

$$\xi_c = \frac{D_2\left[\dfrac{D_1}{(\ell_n \chi_{sc})^{\frac{5}{2}}\chi_{sc}^2} + \dfrac{B(\chi_{sc})}{\chi_{sc}}\right]}{\dfrac{A(\chi_{sc})}{\chi_{sc}} + B(\chi_{sc})} \tag{54}$$

One obstacle here is that we cannot explicitly give the nondimensional sheath thickness χ_{sc} in the above equation. It is obtained only by integrating Eq. (41) from $\xi = 0$. The critical sheath radius χ_{sc} is the value where the sheath increases rapidly from the collisionless value. We place our emphasis here on understanding the parametric dependence of the critical neutral density, and we approximate χ_{sc} by the value at the collisionless limit, that is, the one given by Eq. (53). Using Eqs. (42) and (53), the constant D_1 in the numerator is approximated by

$$D_1 = \frac{1}{0.4\sqrt{2}}\left(\frac{\chi_s - 1}{0.91}\right)^{2.38} \tag{55}$$

Then the critical condition is rewritten as

$$\xi_c = \frac{D_2\left[2.2\dfrac{(\chi_s - 1)^{2.38}}{(\ell_n \chi_s)^{\frac{5}{2}}\chi_s^2} + \dfrac{B(\chi_s)}{\chi_s}\right]}{\dfrac{A(\chi_s)}{\chi_s} + B(\chi_s)} \tag{56}$$

Physically, the first term in the bracket of the numerator corresponds to the electric field increase at the cylinder surface, and the second term corresponds to the increase of ambient charge, $\int (n_e - n_{ai})\, dr$. The denominator corresponds to the increase of the secondary ions. In the thick-sheath limit, $\chi_s \gg 1$, the first term in the numerator can be approximated by 0.3. Then, using Eqs. (49) and (50), we can rewrite Eq. (56) as

$$\xi_c = D_2\left(\frac{0.3 + \sqrt{2}/2}{\sqrt{\pi}/4\chi_s + \sqrt{\pi}/2\chi_s}\right) = 0.8\frac{D_2}{\chi_s} \quad \text{for} \quad \chi_s \gg 1 \tag{57}$$

In the thin-sheath limit, $\chi_s - 1 \ll 1$, we can neglect the second term in the numerator of Eq. (56) because $B(\chi_s)/\chi_s = \sqrt{(\chi_s - 1)} \ll 1$ from Eq. (52). Then, using Eqs. (51) and (52), we have

$$\xi_c = 2.2D_2\frac{(\chi_s - 1)^{2.38}}{(\ell_n \chi_s)^{\frac{5}{2}}\chi_s^2}\frac{1}{(\chi_s - 1)^{\frac{3}{2}} + \chi_s(\chi_s - 1)^{\frac{1}{2}}}$$

$$\approx 2.2D_2\frac{(\chi_s - 1)^{2.38}}{(\chi_s - 1)^3\chi_s^3} = \frac{2.2D_2}{(\chi_s - 1)^{0.62}} \quad \text{for} \quad \chi_s - 1 \ll 1 \tag{58}$$

Using Eqs. (39), (40), (43), and (53), we rewrite Eqs. (57) and (58) in dimensional form. Then the critical neutral density in the real dimensions is given by

$$n_{nc} = 0.9\sqrt{\frac{m_e}{m_i}}\sigma_i^{-1}\lambda_D^{-0.84}r_p^{-0.16}\left(\frac{\kappa T_e}{e\phi_p}\right)^{0.63} \quad \text{for} \quad r_s \gg r_p \tag{59}$$

$$n_{nc} = 2.3\sqrt{\frac{m_e}{m_i}}\sigma_i^{-1}\lambda_D^{-0.52}r_p^{-0.48}\left(\frac{\kappa T_e}{e\phi_p}\right)^{0.39} \quad \text{for} \quad r_s \approx r_p \tag{60}$$

We plot the critical neutral density given by Eq. (56) in Figs. 4 and 5. Figure 4 shows the critical neutral density for three different plasma densities used in Fig. 3. The sheath radius r_s that is used to evaluate the integral is also shown. The electron temperature

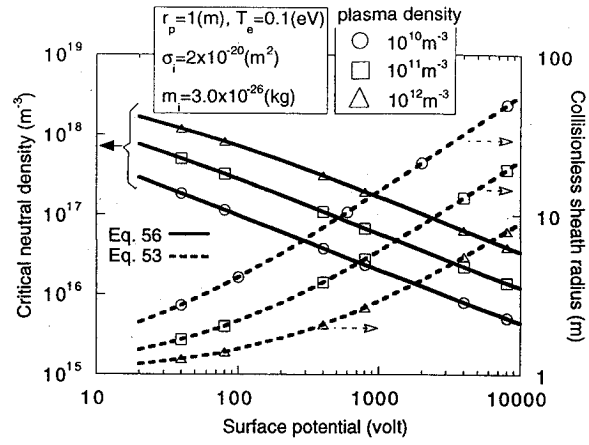

Fig. 4 Critical neutral density and sheath radius for various cylinder surface potentials ϕ_p.

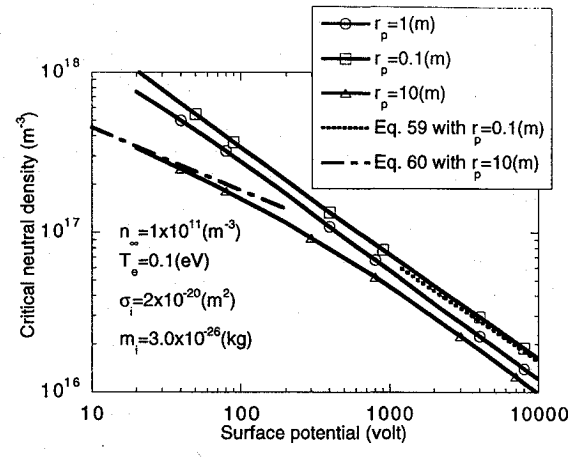

Fig. 5 Critical neutral density for various cylinder surface potentials ϕ_p.

is 0.1 eV, and the cylinder radius is chosen to be 1 m. The ion mass is $m_i = 3.0 \times 10^{-26}$ kg (water vapor), and the ionization cross section $\sigma_i = 2 \times 10^{-20}$ m^2 is assumed. The lower plasma density gives the lower critical neutral density because it gives a thicker sheath, causing more ionization. The critical neutral density lies between 10^{18} and 10^{16} m^{-3}. This level of neutral contamination around a spacecraft is not unrealistic. Therefore, further study is needed to make a more accurate prediction.

Figure 5 shows the dependence of the critical neutral density on the cylinder radius where the plasma density is $n_\infty = 10^{11}$ m^{-3} and the electron temperature is $T_e = 0.1$ eV. In the figure, we also plot the two limiting cases given by Eqs. (59) and (60). For the small cylinder radius $r_p = 0.1$ m and a large potential, the sheath structure approaches the thick-sheath limit, $\chi_s - 1 \gg 1$. Then the power scaling of n_{nc} to ϕ_p approaches -0.63 as given by Eq. (59). On the other hand, as the cylinder radius r_p increases and the potential ϕ_p decreases, the sheath structure approaches the thin-sheath limit, $\chi_s - 1 \ll 1$. Then the power scaling of n_{nc} to ϕ_p approaches -0.39 as given by Eq. (60).

MC-PIC Simulation and Discussion

In this section we employ a MC-PIC code to check the validity of the results in the previous section. The MC-PIC code used in this paper was originally developed by Cho to calculate the arcing onset phenomena on high-voltage solar arrays.[14] The details of the code are described in Ref. 15. The code is one dimensional in space (r direction only) and three dimensional in velocity (v_r, v_θ, v_z). As the neutral species we consider water vapor (H_2O) and use a realistic set of collision cross-section data. The cross sections for elastic vibrational excitation, electronic excitation, ionization, attachment, and charge transfer are tabulated at every 0.1 eV of the collision energy up to 1000 eV. The differential cross sections are

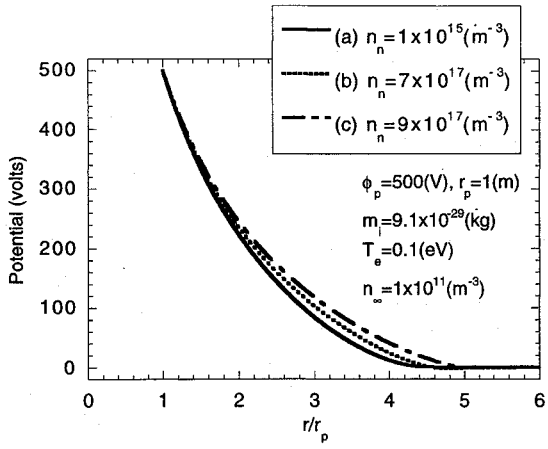

Fig. 6 MC-PIC result of electric potential variations inside the sheath.

also included for calculating the after-collision particle velocity and energy. A test of the quantitative accuracy of the cross-section data is made by calculating the electron swarm and ion drift properties.[15] The coordinate system is the same one as shown in Fig. 1. We assume a Maxwellian plasma outside the computational domain and inject the electrons and ions from the outer boundary according to the thermal flux. At the inner boundary, the potential is held at a constant value ϕ_p, and all the particles that hit the inner boundary are absorbed and leave no charge on the surface.

The ion-to-electron mass ratio is 100. The artificial ion masses can speed up the computation, but at the same time we lose time accuracy. The purpose of the MC-PIC simulation in the present paper is to study whether a stable steady-state sheath structure is possible and the neglect of time accuracy is justified. Also, Eq. (41) contains the effect of the mass ratio in the form of $\sqrt{(m_e/m_i)}$. Therefore, if we substitute $D_2 = \sqrt{(m_e/m_i)} = 0.1$, we can directly compare the result given by the previous cold-fluid analysis with the particle simulation results.

Curve (a) in Fig. 6 shows the steady-state potential for the case of $\phi_p = 500$ V, $r_p = 1$ m, $n_\infty = 1 \times 10^{11}$ m^{-3}, $T_e = 0.1$ eV, $T_i = 0.1$ eV, $n_n = 10^{15}$ m^{-3}. The initial condition for the simulation is given by loading the Maxwellian plasma with n_∞, T_e, and T_i. The number of grids in the computational domain is 625. Each grid cell corresponds to $\Delta r = 0.008$ mm. The inner boundary (the spacecraft surface) is biased suddenly to the potential ϕ_p at $t = 0$. After some transient time, the plasma reaches the steady state. The steadiness is judged by monitoring the current collected by the surface. The sheath structure shown as curve (a) in Fig. 6 corresponds to $\omega_{pe}t = 3700$.

Using the sheath structure shown as curve (a) in Fig. 6 as the initial condition, we now vary the uniform neutral density. Curves (b) and (c) in Fig. 6 show the sheath structures after they reach the steady state. The cases other than $n_n = 10^{15}$ m^{-3} use the plasma condition at $\omega_{pe}t = 3700$ for $n_n = 10^{15}$ m^{-3} as the initial condition. It is as if the neutral density were suddenly increased at $\omega_{pe}t = 3700$. As we increase the density beyond $n_n = 2.5 \times 10^{17}$ m^{-3}, the sheath boundary begins to expand outward. A steady sheath structure is still possible up to $n_n = 9 \times 10^{17}$ m^{-3}. As the density increases beyond $n_n = 1 \times 10^{18}$ m^{-3}, however, the sheath boundary keeps increasing and exceeds the computational boundary. Therefore, it is concluded that the critical neutral density lies somewhere between 9×10^{17} and 1×10^{18} m^{-3}.

In Fig. 7, we show the steady-state sheath radius calculated by the MC-PIC simulations. The sheath radius is determined as the point where the radial electric field becomes zero as seen at the cylinder surface. Inside the sheath the electric field $-d\phi/dr$ is positive everywhere. The points shown in Fig. 7 are the time-averaged values. The points of zero electric field fluctuate to some extent because of the plasma fluctuation outside the sheath boundary. Therefore, we put error bars on the points in Fig. 7, which indicate the standard deviation of the zero-field positions. In the figure we also plot the sheath radius calculated by integrating Eq. (41) from $r_s = 4.17$ m at $n_n = 10^{15}$ m^{-3} with $D_2 = 0.1$. The initial condition is determined by Eq. (53).

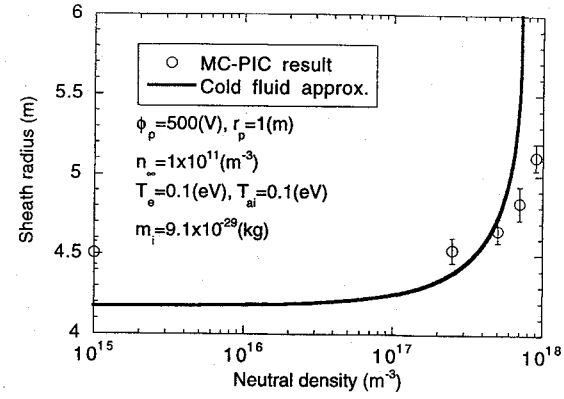

Fig. 7 Comparison of sheath radius.

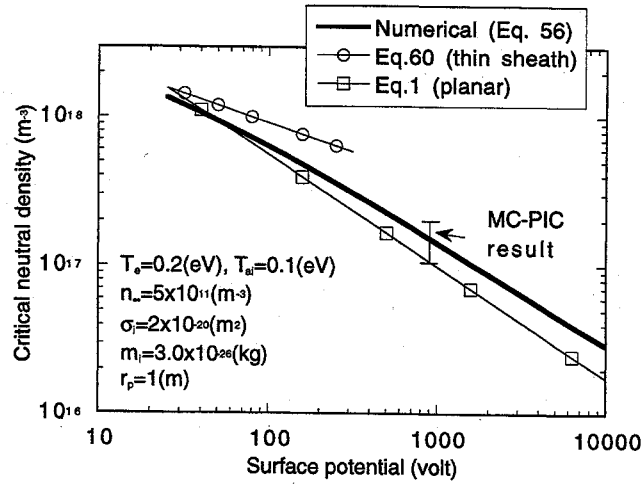

Fig. 8 Comparison of critical neutral density.

The prediction made by the cold-fluid analysis agrees very well with the particle simulation result. The cold-fluid approximation predicts the sheath explosion at $n_n = 7 \times 10^{17}$ m^{-3}, and the MC-PIC simulation shows the explosion between 9×10^{17} and 1×10^{18} m^{-3}. It is only a matter of seconds on a desk top computer to integrate Eq. (41) and find the critical neutral density. On the other hand, it takes days for the particle simulation to calculate all the cases shown in Fig. 7. Since the cold-fluid analysis gives the prediction with error less than one order of magnitude, it is a reasonable tool for calculating the critical neutral density.

To compare the present result with the work of Cooke and Katz,[7] we plot the critical neutral densities calculated by Eqs. (1) and (56) in Fig. 8. In the figure we also plot the result obtained from an MC-PIC simulation where the parameters are different from the one shown in Fig. 7. In this MC-PIC simulation, the mass ratio $m_e/m_i = 0.01$ is used and the space charge due to the secondary ions is corrected by a method described in Ref. 15 to adjust the result to real mass ratio $m_e/m_i = 3.0 \times 10^{-5}$. In the figure, the thick curve is calculated from Eq. (56) by evaluating the functions $A(\chi_s)$ and $B(\chi_s)$ numerically. The thin-sheath limit is calculated by Eq. (60).

The curve by Eq. (56) again agrees very well with the MC-PIC simulation, which shows the validity of the cold-fluid analysis. At a low surface potential, the sheath is thin and the curve of Eq. (56) approaches the limit given by Eq. (60), which has the scaling of -0.39 to the surface potential. The prediction given by Eq. (1) is for the planar geometry and should be compared with the thin-sheath limit. The thin-sheath limit given by Eq. (60) has the power scaling of -0.39 to the surface potential instead of -0.75 for the planar prediction, though the critical neutral densities agree for this particular case at low voltage. The difference in the scalings comes from the fact that we used the single formula given by Eq. (53) to express the parametric dependence of the sheath thickness to derive Eq. (60) from Eq. (58). Equation (58) can also be written as

$$\xi_c = \frac{D_1 D_2}{(\chi_s - 1)^3} \tag{61}$$

For the extremely thin case where $\lambda_D \ll r_p$, we can approximate the geometry as planar and the sheath thickness $r_s - r_p$ should have a scaling of

$$\frac{r_s - r_p}{r_p} \propto \left(\frac{\lambda_D}{r_p}\right)\left(\frac{e\phi}{\kappa T_e}\right)^{\frac{3}{4}} \tag{62}$$

instead of Eq. (53). Then, using Eqs. (39), (40), (42), (43), and (62), the critical neutral density should reduce to the same scaling as Eq. (1):

$$n_{nc} \propto \sqrt{\frac{m_e}{m_i}}\sigma_i^{-1}\lambda_D^{-1}\left(\frac{\kappa T_e}{e\phi_p}\right)^{\frac{3}{4}} \tag{63}$$

Conclusion

The use of high voltage in future space missions requires research on the subject of spacecraft environmental interactions. To determine the spacecraft ground potential, it is essential to know the current–voltage characteristic of the spacecraft surface with a high electric potential. In the present paper we have studied the sheath structure around a cylindrical spacecraft biased to a positive potential and surrounded by a water-vapor cloud with a uniform density. The sheath structure determines the amount of current the spacecraft collects from the ambient plasma.

An explosive sheath expansion can occur if the neutral density around the spacecraft body exceeds a certain value and the spacecraft surface has a positive high potential. Once ionization occurs inside the sheath, the secondary ions stay longer in the sheath than the secondary electrons, because of their low mobility. The electric sheath boundary expands outward to compensate for the relative loss of the negative charge, and above a certain degree of ionization the boundary expands infinitely. We have carried out a cold-fluid analysis to derive an expression for the critical neutral density above which such an explosive sheath expansion occurs for a given set of parameters. For typical conditions, the critical neutral density lies between 10^{16} and 10^{18} m^{-3}, which is not an unrealistic range in the contaminated near-spacecraft environment.

An MC-PIC simulation has been carried out to check the quantitative accuracy of the cold-fluid analysis. The simulation shows that the sheath boundary really expands outward once a sufficient amount of ionization occurs inside the sheath. The MC-PIC result indicates the cold-fluid analysis can predict the critical neutral density with the error less than one order of magnitude. Since it takes only a matter of seconds on a desktop computer to calculate the critical neutral density by the analytical expression derived in the present paper, it can serve as an easy reference in future work.

In the present paper, we have neglected the effects of magnetic field, which might affect the electron motion inside the sheath drastically. This issue should be studied in future work.

Appendix: Collisionless Sheath Thickness

In this appendix we calculate the sheath thickness around a cylindrical object. We consider a case where the electric potential is so high that the orbital motion of particle can be neglected. Using the same coordinate system as the one shown in Fig. 1, we solve the following equations:

$$v_e\frac{\partial v_e}{\partial r} = \frac{e}{m_e}\frac{\partial \phi}{\partial r} \tag{A1}$$

$$\frac{1}{r}\frac{\partial}{\partial r}\left(r\frac{\partial \phi}{\partial r}\right) = -\frac{e}{\epsilon_0}\left[n_0 \exp\left(-\frac{e\phi}{\kappa T_{ai}}\right) - \frac{n_0 v_0 r_s}{v_e r}\right] \tag{A2}$$

The boundary conditions are $\phi(r_p) = \phi_p$, $v_e(r_s) = v_0 = -\sqrt{(\kappa T_e/m_e)}, \phi(r_s) = 0, \partial\phi/\partial r(r_s) = 0$. We nondimensionalize the variables in the following manner:

$$\psi = \frac{\phi}{\phi_p}, \qquad v = \frac{v_e}{\sqrt{2e\phi_p/m_e}}, \qquad z = \frac{r_p}{r}, \qquad z_s = \frac{r_p}{r_s}$$

Then the differential equations (A1) and (A2) are reduced to the following single differential equation:

$$\frac{\partial^2}{\partial z}\psi + \frac{1}{z}\frac{\partial}{\partial z}\psi = -\frac{a_3^2}{a_1^{1.5}}\left[\frac{\sqrt{a_1}}{z^4}\exp\left(-\frac{a_1}{a_2}\psi\right) - \frac{1}{z_s z^3\sqrt{1/a_1 + 2\psi}}\right] \tag{A3}$$

where the nondimensional parameters a_1, a_2, and a_3 are given by

$$a_1 = \frac{e\phi_p}{\kappa T_e}$$

$$a_2 = \frac{T_{ai}}{T_e}$$

$$a_3 = \frac{r_p}{\sqrt{\epsilon_0 \kappa T_e/(n_0 e^2)}}$$

The boundary conditions are $\psi(z_s) = 0$ and $\partial\psi/\partial z(z_s) = 0$. We assume some z_s between 0 and 1 and numerically integrate Eq. (A3) from $z = z_s$ to $z = 1$. This is repeated until we find z_s that gives $\psi = 1$ at $z = 1$. We use the fourth-order Runge–Kutta method, and the iteration is repeated until the error $|\psi(z = 1) - 1|$ becomes less than 0.001.

We plot the numerical result in Fig. A1. In the figure we plot the sheath thickness $(r_s - r_p)/r_p$ against the nondimensional parameter $a_3^2/a_1^{1.5}$, for 1600 combinations of the parameters within the ranges $10^3 < a_1 < 10^5$, $0.1 < a_2 < 1$, $10 < a_3 < 10^4$. The results shown in Fig. A1 can be approximated by

$$\frac{r_s - r_p}{r_p} = 0.62\left(\frac{a_3^2}{a_1^{1.5}}\right)^{-0.42} \tag{A4}$$

This formula gives an approximation of the numerical results shown in Fig. A1 within an error of 2% on average and 11% at maximum.

We also can calculate the electric field at the cylinder surface by integrating Eq. (A3). The use of Eq. (12), which approximates the cylinder surface field by the electric field at zero space charge, underestimates the cylinder surface field and leads to an underestimate of the critical neutral density. The result indicates that Eq. (12) is a good approximation for large a_1, small a_2, and small a_3, that is, a thick-sheath. In the limit of $a_1 = 10^5, a_2 = 0.1$, and $a_3 = 10$, which gives thick-sheath limit, Eq. (12) underestimates the surface field by only 9%. This error leads to only 3% error in the numerical factor of the critical neutral density given by Eq. (59). In the opposite limit of $a_1 = 10^3$, $a_2 = 1$, and $a_3 = 10^4$, which corresponds to the thin-sheath limit, Eq. (12) underestimates the surface field by 59%. This leads to a 59% error of the critical neutral density given by Eq. (60). Since we are mostly concerned with a case of high voltage, that is, large a_1 and a thick sheath, the use of Eq. (12) causes only a minor error in the estimate of the critical neutral density.

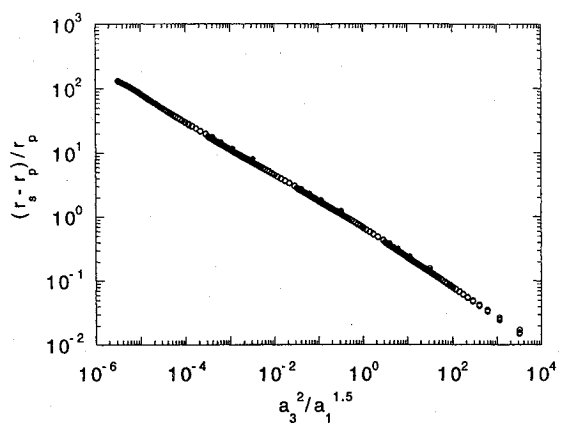

Fig. A1 Nondimensional sheath thickness.

References

[1]Laframboise, J. G., and Sonmar, L. J., "Current Collection by Probes and Electrodes in Space Magnetoplasmas: A Review," *Journal of Geophysical Research*, Vol. 98, No. A1, 1993, pp. 337–357.

[2]Laframboise, J. G., "Theory of Spherical and Cylindrical Langmuir Probes in a Collisionless, Maxwellian Plasma at Rest," Univ. of Toronto, TR, UTIAS Rept. 100, 1966.

[3]Wulf, E., and von Zahn, U., "The Shuttle Environment: Effects of Thruster Firings on Gas Density and Composition in the Payload Bay," *Journal of Geophysical Research*, Vol. 91, No. A3, 1986, pp. 3270–3278.

[4]Myers, N. B., Raitt, W. J., White, A. B., Banks, P. M., Gilchrist, B. E., and Sasaki, S., "Vehicle Charging Effects During Electron Beam Emission from the CHARGE-2 Experiment," *Journal of Spacecraft and Rockets*, Vol. 27, No. 1, 1990, pp. 25–37.

[5]Dobrowolny, M., and Melchioni, E., "Electrodynamic Aspects of the First Tethered Satellite Mission," *Journal of Geophysical Research*, Vol. 98, No. A8, 1993, pp. 13,761–13,778.

[6]Allred, D. B., Benson, J. D., Cohen, H. A., Raitt, W. J., Burt, D. A., Katz, I., Jongeward, G. A., Antoniades, J., Alport, M., Boyd, D., Nunnally, W. C., Dillon, W., Picket, J., and Torbett, R. B., "The SPEAR-I Experiment: High Voltage Effects on Space Charging in the Ionosphere," *IEEE Transactions on Nuclear Science*, Vol. 35, No. 6, 1988, pp. 1386–1393.

[7]Cooke, D. L., and Katz, I., "Ionization-Induced Instability in an Electron Collecting Sheath," *Journal of Spacecraft and Rockets*, Vol. 25, No. 2, 1988, pp. 132–138.

[8]Ma, T. Z., and Schunk, R. W., "Ionization in the Magnetized Ionosphere Surrounding a High Voltage Sphere," *Planetary Space Science*, Vol. 39, No. 10, 1991, pp. 1325–1342.

[9]Greaves, R. G., Boyd, D. A., Antoniades, J. A., and Ellis, R. F., "Steady-State Toroidal Plasma Around a Spherical Anode in a Magnetic Field," *Physical Review Letters*, Vol. 64, No. 8, 1990, pp. 886–889.

[10]Alport, M. J., Antoniades, J. A., Boyd, D. A., Greaves, R. G., and Ellis, R. F., "Electrical Breakdown at Low Pressure in the Presence of a Weak Magnetic Field," *Journal Geophysical Research*, Vol. 95, No. A5, 1990, pp. 6145–6153.

[11]Antoniades, J., Alport, M., Boyd, D., and Ellis, R., "Vacuum-Chamber Testing of Space-Exposed SPEAR-I HV Components," *IEEE Transactions on Electrical Insulation*, Vol. 25, No. 3, 1990, pp. 563–567.

[12]Cho, M., "Crossed Magnetic Field Gas Breakdown Around a Cylindrical Spacecraft in the Ionosphere," *Journal of Physics D: Applied Physics*, Vol. 26, Sept. 1993, pp. 1398–1407.

[13]Parrot, M. J. M., Storey, L. R. O., Parker, L. W., and Laframboise, J. G., "Theory of Cylindrical and Spherical Langmuir Probes in the Limit of Vanishing Debye Number," *Physics of Fluids*, Vol. 25, No. 12, 1982, pp. 2388–2400.

[14]Cho, M., and Hastings, D. E., "Computer Particle Simulation of High Voltage Solar Array Arcing Onset," *Journal of Spacecraft and Rockets*, Vol. 30, No. 2, 1992, pp. 189–201.

[15]Cho, M., and Hastings, D. E., "An Analytical and Particle Simulation Study of Localized Semi-Vacuum Gas Breakdown Phenomena on High Voltage Solar Surfaces in Low Earth Orbit," *Physics of Fluids B*, Vol. 4, No. 8, 1992, pp. 2614–2625.

A. L. Vampola
Associate Editor